The nonlinear dynamic behavior of a Rubber-Layer Roller Bearing (RLRB) for vibration isolation

(Article begins on next page)

18 April 2024

The non-linear dynamic behavior of a Rubber-Layer Roller Bearing (RLRB) seismic isolator

N. Menga,[1, 2, *] F. Bottiglione,[1] and G. Carbone[1, 2, 3]

[1]*Department of Mechanics, Mathematics and Management,*
Politecnico of Bari, V.le Japigia, 182, 70126, Bari, Italy
[2]*Imperial College London, Department of Mechanical Engineering,*
Exhibition Road, London SW7 2AZ
[3]*CNR - Institute for Photonics and Nanotechnologies U.O.S. Bari,*
Physics Department "M. Merlin", via Amendola 173, 70126 Bari, Italy

Abstract

In this paper, we study the dynamic behavior of a Rubber-Layer Roller Bearing (RLRB) interposed between a spring-mass elemental superstructure and a vibrating base. Thanks to the viscoelastic rolling contact between the rigid rollers and the rubber layers, the RLRB is able to provide a nonlinear damping behavior. The effect of the RLRB geometric and material parameters is investigated under periodic base excitation, showing that both periodic and aperiodic responses can be achieved. Specifically, when the motion involves the decreasing portion of the damping curve, strongly nonlinear phenomena affect the system dynamics. Further, focusing on the mean shock of the Central Italy 2016 earthquake, we perform a material and geometrical optimization of the RLRB. The results show that significant reduction of both the peak and root-mean-square value of the inertial force acting on the superstructure is achieved, compared to the best performance of a linear base isolation system.

---

*Electronic address: [Correspondingauthor.]Email:nicola.menga@poliba.it,phonenumber: +390805962746

I. INTRODUCTION

Absorbing and controlling the vibration of mechanical systems and structure is a very demanding task. Due to the always increasing demand from mechanical, aeronautical and civil engineering, the last decades have seen a proliferation of applications of non-linear systems to vibration control, thanks to their intrinsic ability (i) to efficiently react to external forcing in a much wider range of frequency compared to linear systems, (ii) to modify their behavior according to the excitation amplitude.

In this view, one of the most common vibration absorbtion strategy relies on the adoption of non-linear energy sinks (NES), whose mechanism depends on the specific field of application. To this regard, in Ref. [1] the effect of the non-linear (quadratic) damping behavior given by an hydraulic damper equipped with several on/off valves is studied, showing that the removal of unwanted periodic regimes can be achieved by means of opportunely tuned damping characteristics. Similar studies were then extended to the case of vibro-impact NES [2, 3], showing that chaotic dynamic regimes are easy to occur, thus promoting these systems for energy harvesting applications. Similarly, focusing on the case of travelling loads on elastic beams (e.g. railway tracks under moving trains), an extensive study on non-linear tuned mass dampers has been performed in Refs. [4–6], showing that stiffness nonlinearity poorly affects the overall dynamic response, whereas non-linear damping may lead to great vibration reduction. Moreover, the case of a moving mass-damper for transmission cables is investigated in Ref. [7], where it is shown that significantly higher energy dissipation can be achieved compared to the case of fixed dampers.

Among the application fields of vibration control, seismic engineering is one of the fastest growing sector, as the ability to ensure high reliability for primary structures and machineries (e.g., power plants, hospitals, schools, etc.) has strong social, political, and economic implications [8]. Therefore, several passive systems have been developed to deal with this task, mostly relying on nonlinear stiffness behavior. Indeed, both inter-story frictional dissipators [9] for high-rise buildings (where the source of nonlinearity are the frictional interactions), and bi-component sacrificial supports [10] able to provide a piecewise linear foundation stiffness have shown general vibration absorption and reduced structure response.

Base isolation systems are also well established methods to control the superstructure dynamic response, as indeed reviewed in Ref. [11]. Among them, very promising solutions relies rolling isolation systems (RIS), where the rolling of rigid balls on concave counterfaces provides a nonlinear gravitational stiffness, and external viscous dashpot provides linear damping. In Refs. [12, 13], it is shown that such devices are peculiarly suited for heavy low-rise structures, presenting significantly enhanced isolation performances. On the same path, the idea to combine passive base isolation with active structural control is investigated in Ref. [14], where several control logics are explored on order to minimize a specific performance index based on absolute acceleration, and inter-story drift and velocity.

On the other hand, less effort has been paid to study in details the dynamic character of such isolation systems. Indeed, only a few works highlighted that, under specific conditions, RIS may show chaotic behavior [15, 16] (mostly due to the vabiable curvature of the rolling counterfaces), thus resulting in significant sensitivity to initial conditions and, in turn, less engineering predictability of the overall isolation behavior.

Furthermore, in order to provide specific nonlinear stiffness and damping, most of the RISs for base isolation systems rely on separated mechanical components [17] (e.g. nonlinear spring, hydraulic dampers with valves, etc.), which need to be arranged in specific, and

usually complex, configurations. This entails high installation and maintenance costs, as well as reduced reliability.
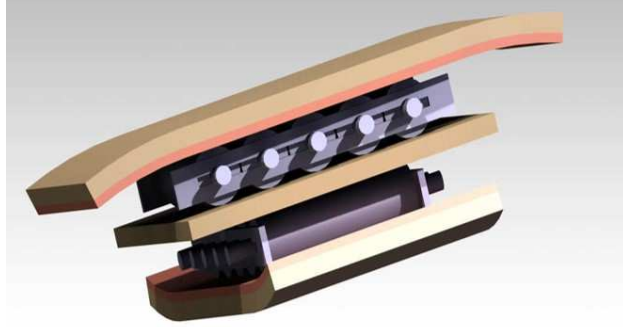

FIG. 1: A representation of a bi-axial cyclindrical RLRB: two rows of equispaced steel rollers are interposed between steel plates coated with rubber layers. The top and bottom plates present slightly concave shapes, in order to provide a gravitational recentering effect (figure from Ref. [24] under copyright agreement)

To overcome these limitations, Rubber-Layer Rolling Bearings (RLRB) have been proposed so far [18 **?** , 19], where the rolling balls counterparts were opportunely coated with highly viscoelastic rubber, thus providing both significant damping without additional devices. Similar studies were later widened to the case of rolling rods in Refs. [22, 23]. Although pioneeristic, these studies do not provide a detailed insight into the viscoelastic bulk dissipation mechanism, and in turn into the damping behavior of such systems, which is instead addressed by means of phenomenological models. To this regard, in a recent paper [24], two of us deeply investigated the damping behavior of an innovative RLRB based on rolling cylinders (see fig. 1), which, showing overall lower contact pressures, provides higher rubber reliability compared to sphere-based RLRB. In the framework of linear viscoelasticity, we accurately defined the damping curve associated to viscoelastic bulk dissipation, assuming steady rolling conditions.

In this paper, we try to widen the investigation of cylindrical RLRBs by studying the dynamic behavior of the exemplar case of a single-story superstructure base isolated by means of a RLRB. The paper is organized in two sections. The first one is devoted to the viscoelastic contact mechanics formulation, based on Boundary Element Method (BEM) with specific viscoelastic Green's function taking into account for the system materials and geometry, together with the dynamical model of the system, where the two degree of freedom equations of motion are derived. In the second section, we present our main results: firstly we focus on the system dynamics under periodic base excitation, highlighting the effect of the RLRB geometrical and material parameters; then, a detailed optimization of the RLRB parameters is performed considering a real earthquake base excitation. To stress the effect of the specific RLRB behavior nonlinearity on the system response, the results are compared with the case of an equivalent linear base isolation device.

II. FORMULATION

A. The RLRB viscoelastic behavior

The damping behavior of the base isolation systems depends on the viscoelastic contact behavior of the RLRB. In fig. 2, we show a portion of the periodic contact between the RLRB equispaced rigid rollers and the viscoelastic layer stuck onto a rigid plate. The relative motion between the top and the bottom plate leads to cyclic deformations of the viscoelastic rubber coating, entailing bulk dissipation which gives rise to a reaction force, opposing the relative motion. In what follows, we assume frictionless contact between the rigid cylinders and the viscoelastic layer of thickness h. Since our study is developed within the framework of linear viscoelasticity, we neglect any large deformation effect. Referring to fig. 2, for a given value of the velocity V, the mean shear stress acting on the upper body can be easily calculated as

$$f_m(V) = -\frac{1}{\lambda} \int_\Omega p(x) u'(x) dx \tag{1}$$

where λ is the periodic distance between the cylinders, $p(x)$ is the contact pressure distribution, and $u'(x)$ the first derivative of the displacement field of the viscoelastic layers within the contact domain $\Omega = [-a, a]$ (see Fig. 2).
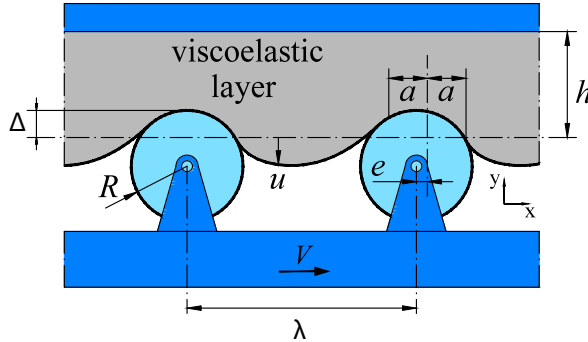

FIG. 2: The geometrical scheme of the periodic rolling contact under investigation: rigid equispaced cylinders (of radius R) are in rolling contact with a viscoelastic layer of thickness h. The latter is rigidly confined on the upper boundary. In particular, Δ is the contact penetration between the cylinders and the deformed surface mean plane, and u is the layer local displacement. Due to the delay in the viscoelstic response of the material, the contact area mean line is shifted by a quantity e with respect to the cylinders axis.

Eq. 1 clearly shows that the overall damping force depends on the contact pressure distribution, which is unknown. Following Ref. [24], by exploiting the symmetry of the system, we focus our study on half of the device, as indeed shown in fig. 2. Furthermore, it can be demostrated that $f_m(V)$ is an odd function of V, as the mean tangential shear stress always opposes the realtive motion between the RLRB upper and lower parts.

Following the procedure delineated in Refs.[24, 25], by relying on the Green's function approach, the displacement and the contact pressure fields can be related by means of a

4

specific Green's function, which, in the case of steady sliding, parametrically depends on V. Thus,

$$u(x) = -\int_{\Omega} \Theta_V(x-s) p(s) \, ds. \tag{2}$$

The kernel $\Theta_V(x)$ is the viscoelastic Green's function for steady sliding contacts, which has been already calculated in the case of periodic contacts with layers of finite thickness in Refs. [26, 27]. We report herein the main relations, assuming linear viscoelastic material with a single relaxation time τ

$$\Theta_V(x) = \frac{1}{E_\infty} G(x) + \frac{1}{E_1} \int_{0^+}^{+\infty} G(x + V\tau z) \exp(-z) \, dz \tag{3}$$

where $1/E_1 = 1/E_0 - 1/E_\infty$, being E_0 and E_∞ respectively the zero-frequency and high frequency elastic moduli of the material. The elastic-like Green's function is related to the specific geometry under investigation, and takes the form

$$G(x) = \frac{2(1-\nu^2)}{\pi} \log\left[2\left|\sin\left(\frac{kx}{2}\right)\right|\right] + \frac{2(1-\nu^2)}{\pi} \sum_{m=1}^{\infty} A_m(kh) \frac{\cos(mkx)}{m} \tag{4}$$

with $k = 2\pi/\lambda$ and

$$A_m(kh) = \frac{2hkm - (3-4\nu)\sinh(2hkm)}{5 + 2(hkm)^2 - 4\nu(3-2\nu) + (3-4\nu)\cosh(2hkm)} + 1 \tag{5}$$

where ν is the material Poisson's ratio.

Fig. 2 shows that, due the viscoelastic delay in the material response, the contact area exhibit a certain degree of eccentricity e with respect to the mean line of the cylinder cross-section. Moreover, within the contact strip Ω, the layer displacement must copy the rigid cylinder shape, i.e. $u(x) = \Delta - \Lambda[1 - r(x+e)]$, where $r(x) = R\sin[\cos^{-1}(x/R)]$ is the profile of the upper half-cylinder, and $\Lambda = R - \lambda^{-1}\int_\lambda r(x) \, dx$. Under these conditions, Eq. (2) represents a Fredholm equation of the first kind which is solved for the unknown contact pressure distribution by exploiting the numerical scheme already discussed in Refs. [28–30] for adhesiveless contacts.

B. The system dynamics

RLRB devices are usually adopted to achieve a certain degree of dynamic base isolation [11] between the ground (e.g. seismic) motion and several superstructures, such as buildings, machinery, etc. Since in this study we are interested in highlighting the dynamic behavior peculiarities of the RLRB system, we focus on a very simple superstructure: an elastic pillar (with bending stiffness k_2) supporting an inertial mass m_2.

A functional scheme of the resulting system is shown in figure 3, together with a lumped element picture of the system. Specifically, we consider the case of a concave RLRB (with radius of curvature $R_b \gg R$), whose gravitational re-centering effect is taken into account by means of a linearized gravitational spring with stiffness

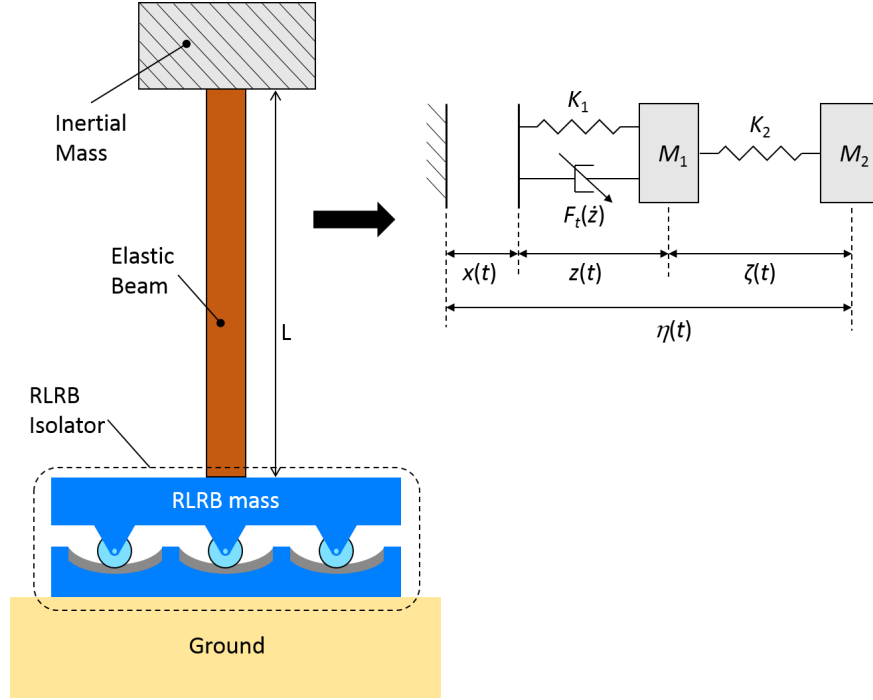$$k_1 = g\frac{m_1 + m_2}{R_b} \tag{6}$$

5

FIG. 3: A sketch of the physical system: an RLRB device is adopted to provide dynamic base isolation between an heavy superstructure and the ground motion. The heavy mass m_2 is connected to the RLRB system by means of an elastic beam of length L and bending stiffness K_2. The RLRB rolling path is concave, thus resulting in a linearized recentering stiffness K_1. A lumped element representation of the same system is given on the right.

where g is the gravitational acceleration.

The dissipation of the viscoelastic rolling contact occurring between the RLRB rigid cylinders and rubber layer leads to a damping tangential force opposing the relative motion between the superstructure and the ground. Such a force can be calculated as

$$F_d\left(\dot{z}\right) = -N\lambda b\left|f_m\left(\dot{z}\right)\right|\frac{\dot{z}}{|\dot{z}|}$$

where N is the number of rigid cylinders of the RLRB device, and b is the transverse width of the systems.

The equations of motion of the system of fig. 3 are

$$\begin{cases} m_1\left(\ddot{x}+\ddot{z}\right)+k_1 z - F_d\left(\dot{z}\right) - k_2\zeta = 0 \\ m_2\left(\ddot{x}+\ddot{z}+\ddot{\zeta}\right)+k_2\zeta = 0 \end{cases} \qquad (7)$$

where $x\left(t\right)$ is the ground vibration. We also define

$$\eta(t) = x(t) + z(t) + \zeta(t) \qquad (8)$$

as the absolute displacement of the inertial mass.

Eqs. (7) represent a set of non-linear second order ODE, which have been integrated numerically by relying on a fixed time-step method based on fourth order *Runge-Kutta*

algorithm [31]. To avoid numerical instabilities, a sensibility study has been performed on the effect of the time-step value on the integration result.

Interestingly, the equilibrium along the vertical direction of the physical system shown in fig. 3 allows us to calculate the contact mean pressure acting on the rigid cylinders-rubber layer interface as

$$p_m = \frac{1}{\lambda} \int_\Omega p(x)\, dx = g \frac{m_1 + m_2}{N \lambda b} \tag{9}$$

Notably, due to the osciallatory shape of the base excitation $x(t)$ typical of seismic and vibrational phenomena, the RLRB undergoes to a reciprocating motion. In this case, the viscoelastic contact between the rubber layer and the rigid cylinders belongs to the class of reciprocating rolling contacts, usually requiring sophisticated theoretical treatments to address the specific frictional and contact behavior. However, in Ref. [32], it has been shown that simplified unidirectional steady motion analysis may still provide good qualitative and quantitative predictions, depending on the actual operating conditions. In particular, once defined the linear size $2a$ of the contact area between the cylinders and the rubber, the stroke s and the period T of the reciprocating motion, the viscoelastic contact behavior closely resembles the one observed in steady sliding at constant velocity provided that $a \ll s$ and $\tau \ll T$. Since in our analysis, the latter conditions are met, we will here approximate the reciprocating viscoelastic response with the equivalent unidirectional steady one.

III. RESULTS

A. Viscoelastic contact behavior

In this section, we present the main results in term of contact conditions experienced at the interface between the rubber layer and the rigid cylinders. Specifically, we consider the case of a single relaxation time incompressible viscoelastic material (i.e. $\nu = 0.5$), whose high and zero frequency elastic moduli are $E_\infty = 150$ MPa and $E_0 = 50$ MPa, respectively.
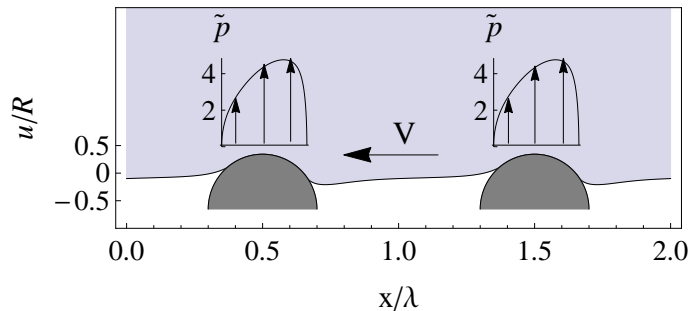

FIG. 4: The deformed contact configuration under rolling at steady velocity. Due to the viscoelasic bulk dissipation, both the displacement and pressure fields are asymmetric, thus resulting in an orizzontal component of the contact force opposing the relative motion.

Fig. 4 shows a typical shape of the deformed layer in steady rolling contact over cylindrical indenters (i.e. the rigid rollers). A certain degree of eccentricity of the contact area with respect to the rigid cylinders meanline is experienced due to the delay in the material response (i.e. the energy dissipation occurring in the bulk viscoelastic material), which, in

turn, also gives rise to asymmetric contact pressure distributions. Although dealing with namely frictionless contact, under these conditions, following Eq. (1), the contact force presents a tangential component (the so-called "viscoelastic friction") which opposes to the relative motion between the cylinders and the rubber layer. Focusing on our physical system (see fig. 3) such a force represent the damping force opposing the motion between the superstructure and the ground.
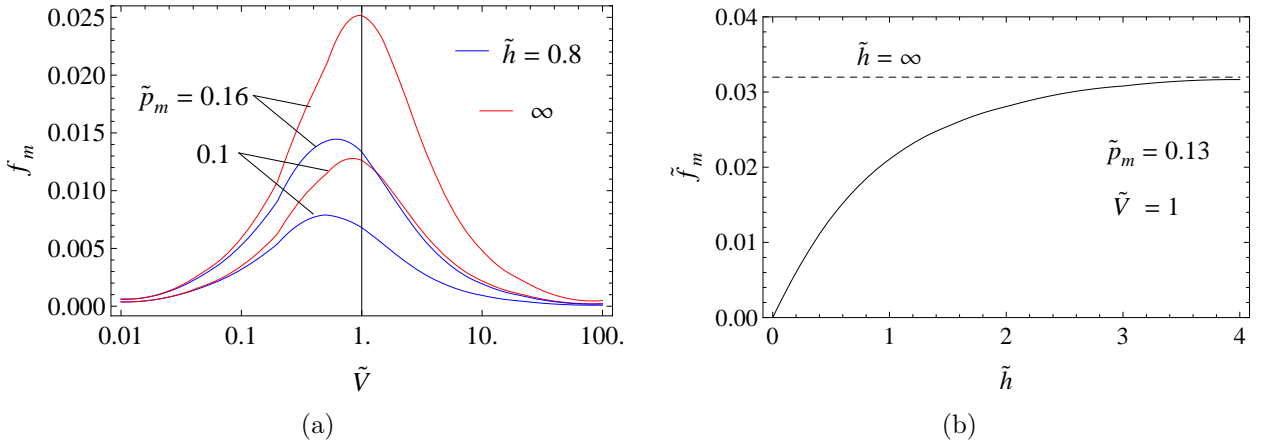

FIG. 5: The dimensionless mean shear stress $\tilde{f}_m$ as a function of (a) the dimensionless relative velocity $\tilde{V}$, and (b) the dimensionless thickness $\tilde{h}$. Results refer to (a) $\tilde{R} = 0.3$, and (b) $\tilde{R} = 0.1$

Figs. 5 show the frictional viscoelastic behavior of the contact. Specifically, from fig. 5a, showing the dimensionless friction mean shear stress $\tilde{f}_m = 2 \left(1 - \nu^2\right) f_m / E_0$ as a function of the dimensionless velocity $\tilde{V} = V \tau k$ for different values of the dimensionless contact mean pressure $\tilde{p}_m = 2 \left(1 - \nu^2\right) p_m / E_0$, we observe that the viscoelastic friction follows the well-known bell shaped curve, as at very high and very low excitation frequency it behaves as an elastic material, with vanishing bulk dissipation. On the contrary, in the range of intermediate frequency, the viscous dissipation plays a key role, and the frictional force arises. This is because the largest viscoelastic energy dissipation, and hence friction, occurs when $Im[E(\omega)]/|E(\omega)|$ is maximized, i.e. at values of $\omega\tau \approx 1$ (see Ref. [26, 27]), where ω is the excitation frequency, and

$$E\left(\omega\right) = E_0 + E_1 \frac{i\omega\tau}{1 + i\omega\tau} \tag{10}$$

is the viscoelastic complex modulus, with $E_1 = E_\infty - E_0$.

Furthermore, from fig. 5a we observe that the thicker the rubber layer, the larger the friction value is, as increasing $\tilde{h}$ the amount of deformed material increases as well, leading to higher bulk dissipation. This is more clearly shown in Fig. 5b, where $\tilde{f}_m$ is plotted as a function of the dimensionless thickness $\tilde{h} = kh$. Of course, increasing the rubber layer thickness, the viscoelastic half-plane behavior (i.e. for $h = \infty$) is asymptotically recovered, whereas, in the limit of vanishing thickness (i.e. for $h \rightarrow 0$), vanishing viscoelastic friction is achieved.

8

B. Dynamic behavior with periodic base excitation

Let us now focus on the dynamic response of the physical system under periodic base excitation in the form $x(t) = A_0 \sin(\omega t)$, where A_0 and ω are, respectively, the amplitude and the frequency of the excitation. The physical system we focus on is typical of seismic engineering, thus we set $m_1 = 1 \times 10^2$ kg, $m_2 = 1 \times 10^5$ kg. We assume a concave shape for the RLRB pathway with width $b = 1$ m, and radius of curvature $R_b = 3.3$ m, which from Eq. 6 gives $k_1 = 3 \times 10^5$ N/m. We also assume $\tilde{h} = 0.8$ and $\tilde{R} = 0.3$. Similarly, the elastic pillar is constituted by a commercial HEB 300 steel beam, with $L = 3$ m, whose bending stiffness is $k_2 = 6 \times 10^6$ N/m. Moving from these values, the modal analysis of the system allows to identify the two natural frequencies $\omega_1 = 1.69$ rad/s, and $\omega_2 = 251$ rad/s.
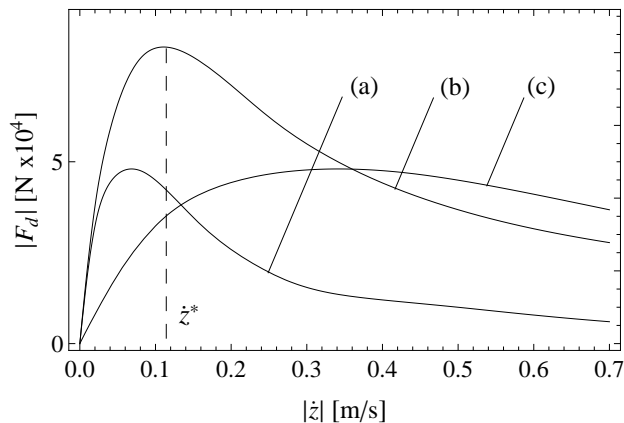

FIG. 6: The absolute value of the viscoelastic damping force F_d as a function of the absolute relative velocity $\dot{z}$ between the ground and the upper plate of the RLRB device. Curve (a) is for $\tau = 0.25$ s, $\lambda = 0.25$ m; curve (b) is for $\tau = 0.05$ s, $\lambda = 0.05$ m; curve (c) is for $\tau = 0.05$ s, $\lambda = 0.25$ m. Notably, the velocity $\dot{z}^*$ corresponding to the peak force is shown only for curve (b).

Regarding the viscoelastic non-linear damping force, coherently with the dimensionless results presented in fig. 5a, we observe that, given the values of $\tilde{h}$ and $\tilde{R}$, the final load-velocity curve depends on both the values of τ and λ. The effect of such parameters on the damping behavior of the RLRB is shown in fig. 6. We observe that reducing the ratio τ/λ leads to lower slope of the curve close to the origin. Similarly, increasing λ causes a reduction of the peak force value as, through Eq. (9), it entails a reduction of the contact mean pressure, thus reducing the overall amount of material involved in the cyclic deformation, and in turn the energy dissipation. Notably, $\dot{z}^*$ defined as the absolute value of the velocity corresponding to the peak force, depends on the specific parameters as well.

Furthermore, for any specific damping curve, it is possible to define an "equivalent" linear viscous damping behavior with damping coefficient

$$c_{eq} = -\left.\frac{dF_d}{dV}\right|_{V=0} \tag{11}$$

Fig. 7 shows the effect of τ and λ on the value of c_{eq}, in a contour plot. We observe that, according to fig. 6, increasing the viscoelastic relaxation time τ, as well as reducing λ, the equivalent damping coefficient increases. Further, in the same figure, three lines have
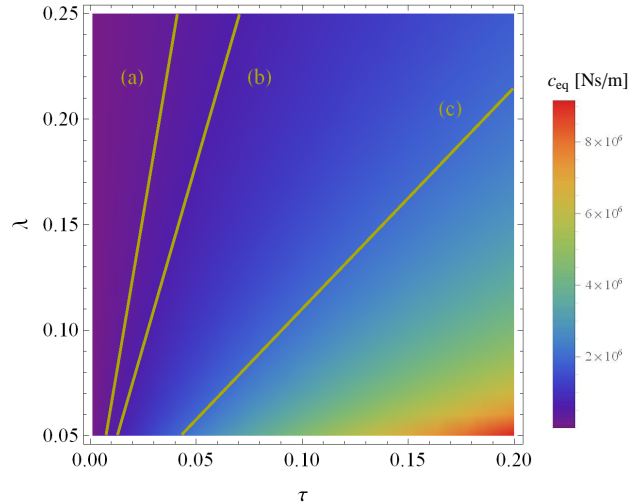
FIG. 7: The equivalent damping coefficient c_{eq} as a function of τ and λ. The three lines are for (a) $c_{eq} = 3.5 \times 10^5$ Ns/m; (b) $c_{eq} = 6 \times 10^5$ Ns/m; (a) $c_{eq} = 2 \times 10^6$ Ns/m;

Case	τ [s]	λ [m]	c_{eq} [Ns/m]	$\dot{z}^*$ [m/s]
(a)	0.00765	0.05	3.5×10^5	0.724
(b)	0.024	0.15	3.5×10^5	0.534
(c)	0.041	0.25	3.5×10^5	0.417
(d)	0.0131	0.05	6×10^5	0.423
(e)	0.0411	0.15	6×10^5	0.312
(f)	0.0702	0.25	6×10^5	0.244
(g)	0.0437	0.05	2×10^6	0.127
(h)	0.12	0.132	2×10^6	0.097
(i)	0.2	0.214	2×10^6	0.081

TABLE I: RLRB characteristics of fig. 8

been added referring to specific values of c_{eq}, each one allowing to determine a sets of τ and λ whose equivalent linear damping behavior is the same. Of course, we expect the system dynamics to be strongly affected by the values of τ and λ, as the strongly non-linear viscoelastic damping of the RLRB may lead to completely different behaviors even in the case of similar linearized equivalent damping coefficients.

This is clearly shown in fig. 8 where nine sets of parameters are investigated, as detailed in Table I. Specifically, each row of figures refers to the same linearized equivalent damping coefficient, increasing from the top to the bottom. The figures show, in the lower part, a contour plot of the steady-state system response spectrum $\bar{\eta}_\omega(\omega_f) = \mathcal{F}(\eta(t, \omega))$ as a function of the excitation frequency ω (where $\mathcal{F}$ is the Fourier trasform operator). Similarly, in the upper part we show, on the left axis, the steady-state maximum amplitude $|\eta|_{\max}$ of the system response for the non-linear (blue histogram) and equivalent linearized (red curve) systems as a function of the excitation frequency ω, whereas on the right axis (black curve) the steady-state maximum amplitude $|\dot{\eta}|_{\max}$ of the system velocity response is shown.

Figures 8a, 8b, 8c share the same linearized behavior (i.e. τ/λ is almost constant) with
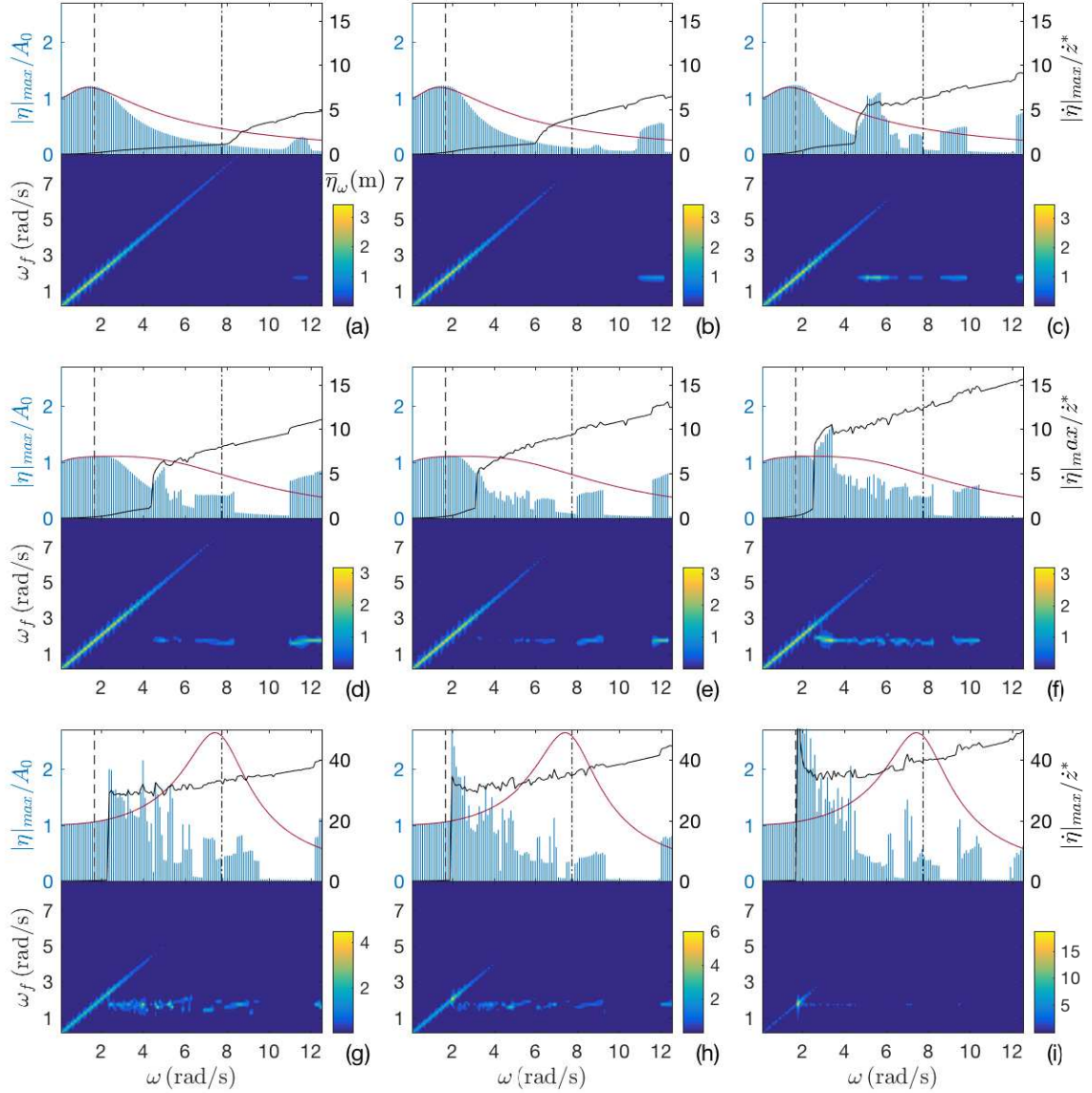
FIG. 8: Upper diagrams: on the left axis, the dimensionless maximum amplitude of the system response $|\eta|_{\max}$ (left axis) for the non-linear (blue istogram) and equivalent linearized (red curve) systems as a function of the excitation frequency ω; on the right axis (black curve) the dimensionless maximum amplitude of the system velocity response $|\dot{\eta}|_{\max}$. Lower contour plots, the system response spectrum $\bar{\eta}(\omega_f)$ as a function of the excitation frequency ω. The values of τ and λ related to each figure are reported in Table I.

maximum amplitude of oscillation close to the system natural frequency ω_1. Interestingly, moving from fig. 8a to 8c the value of λ increases (see the data in Table I) thus the non-linear damping force peak value reduces. This entails that the larger the value of λ, the smaller the value of ω at which the system operating conditions overcome the damping force peak threshold velocity $\dot{z}^*$. Indeed, strongly non-linear effects usually occurs only at sufficiently

11

large values of ω where the system response involves $|\dot{z}|_{\max} > \dot{z}^*$ (i.e. on the decreasing portion of the damping force curve of fig. 6); whereas, at sufficiently small value of ω, the nonlinear system vibration closely resembles the one of the linearized system.

Such a peculiar behavior is even more clearly shown by figures 8g, 8h, 8i, all referring to a set of τ and λ associated to a very high value of linearized equivalent damping coefficient c_{eq}. Under these conditions, since the linear viscous damper behaves almost rigidly, the linear system behavior (see the red curves) closely resembles the one of a one degree of freedom harmonic oscillator, of undamped mass m_2 and stiffness k_2 (i.e. maximum amplitude of oscillation close to the natural frequency $\sqrt{k_2/m_2} = 7.75$ rad/s). The non-linear system behaves differently. Indeed, for the specific parameters, the non-linear damping force peak value is reached even for low excitation frequency, and strong non-linear effects occurs. Notably, from the system response spectrum shown in the lower contour plots, we observe that the overall response of the non linear system always involves a harmonic term associated to the external periodic excitation, whereas the main effect of the non-linear damping is to "chaotically" switch on the harmonic term related to the low natural frequency ω_1.

Figure 9 illustrates the system behavior of case (d) of Table I at different excitation frequencies. Both the system response time histories, phase portraits and Poincaré maps refers to the steady-state conditions. The Poincaré maps (or recurrence maps) have been achieved by sampling the system response at intervals equal to the excitation period, with random phase.

According to fig. 8d, at $\omega = 1.5$ rad/s the system behaves linearly with a periodic response, thus the Poincaré map is simple point, and the phase portrait is an ellipse.

Increasing ω up to 4 rad/s, non-linear damping starts to play a non-vanishing role. The system response is still periodic, but the phase portrait is now a deformed ellipse.

At $\omega = 4.9$ rad/s the system response involves $|\dot{z}|_{\max} > \dot{z}^*$ (see fig. 8d). Under these conditions, the vibration spectrum is the sum of two main incommensurable harmonics: the first excitation harmonic ω, and the system low natural frequency ω_1. As a consequence, the resulting Poincaré map is a closed curve, whereas the phase portrait is not, filling a portion of the phase space.

A slight increase of ω up to 5.1 rad/s leads to different results. This time the ratio of the main frequencies of the system response spectrum is an integer number, as $\omega/\omega_1 \approx 3$. Since the response is periodic the phase portrait is a closed curve, and the Poincaré map shows the same number of isolated points such as the ratio ω/ω_1. A similar behavior is also shown at $\omega = 6.8$ rad/s and $\omega = 11.8$ rad/s, where respectively $\omega/\omega_1 \approx 4$ and $\omega/\omega_1 \approx 7$

Increasing ω up to 12.5 rad/s, the two main components become incommensurable, the system dynamics is not periodic and a closed curve is observed in the Poincaré map associated with a colored region in the phase portrait.

IV. OPTIMIZATION OF THE RLRB DYNAMIC BEHAVIOR

In the previous section it has been clearly pointed out that the dynamic behavior of the physical system is strongly affected by the specific damping behavior of the RLRB base isolation device. Since the latter depends, in turn, by the specific choice of the physical parameters τ and λ, it is evident that a fine tuning can be performed in order to optimize the overall behavior of the system with respect to a performance index.

To stress the impact of our conclusions, in what follows, we focus on a real seismic event, namely the main shock of the Central Italy earthquakes [37] occurred on October 30th 2016,
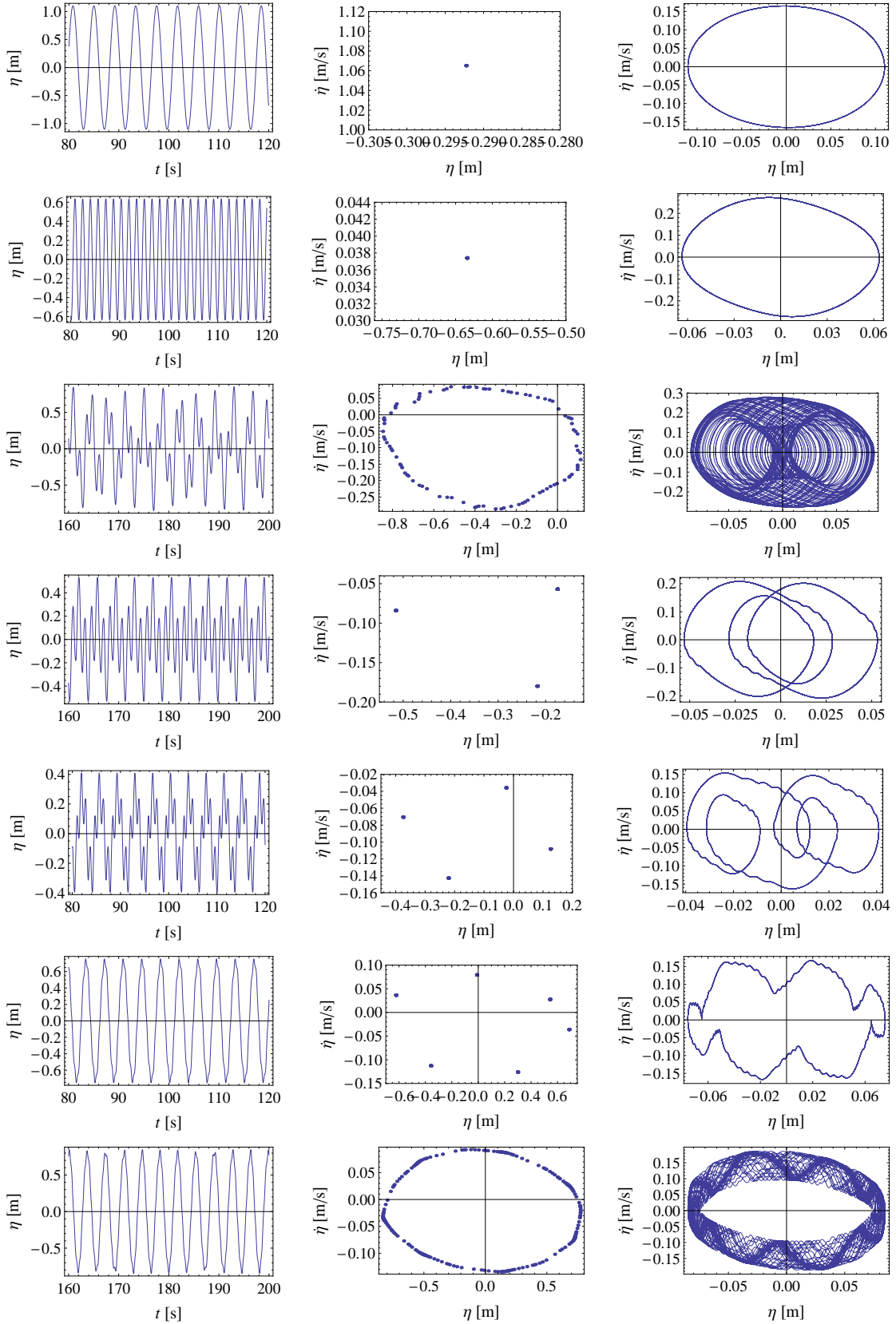
FIG. 9: The system dynamic behavior for case (d) of Table I, at varying excitation frequency ω.

13

with magnitude 6.6 M_w. In terms of performance indexes, most of the previous studies focuses on multi-story superstructure [33], in which the main source of damage is the inter-story drift, leading to critical shear stresses, and eventually to the structural collapse. In these cases, the most adopted performance indexes are the relative velocity and displacement of each story [34, 35]. However, since our work is more fundamental, we define a performance index ϕ which encompasses two source of damage for the structural elements (i.e. the elastic beam of our system): (i) the maximum inertial load F_M^i on the mass m_2, associated to the structure instantaneous damage [36]; (ii) the root mean square F_{rms}^i of the inertial loads history during the shake, associated to the material hysteresis and fatigue. Specifically, we have that

$$\phi = \frac{1}{2}\left(\frac{F_M^i}{F_{M,0}^i} + \frac{F_{rms}^i}{F_{rms,0}^i}\right) \tag{12}$$

where

$$F_M^i = m_2 \ddot{\eta}_M \tag{13}$$

being $\ddot{\eta}_M$ the absolute acceleration maximum, and

$$F_{rms}^i = m_2 \sqrt{\int_{t_1}^{t_2} \frac{\ddot{\eta}(t)^2}{t_2 - t_1} dt} \tag{14}$$

The optimization strategy is the following. Firstly, single objective minimization of $F_M^i(\tau, \lambda)$ and $F_{rms}^i(\tau, \lambda)$ are set independently. The homogeneization terms $F_{M,0}^i$ and $F_{rms,0}^i$, in Eq. (12), are then defined as the corresponding values in single objective optimized conditions. Finally, the minimization of $\phi(\tau, \lambda)$ is performed.
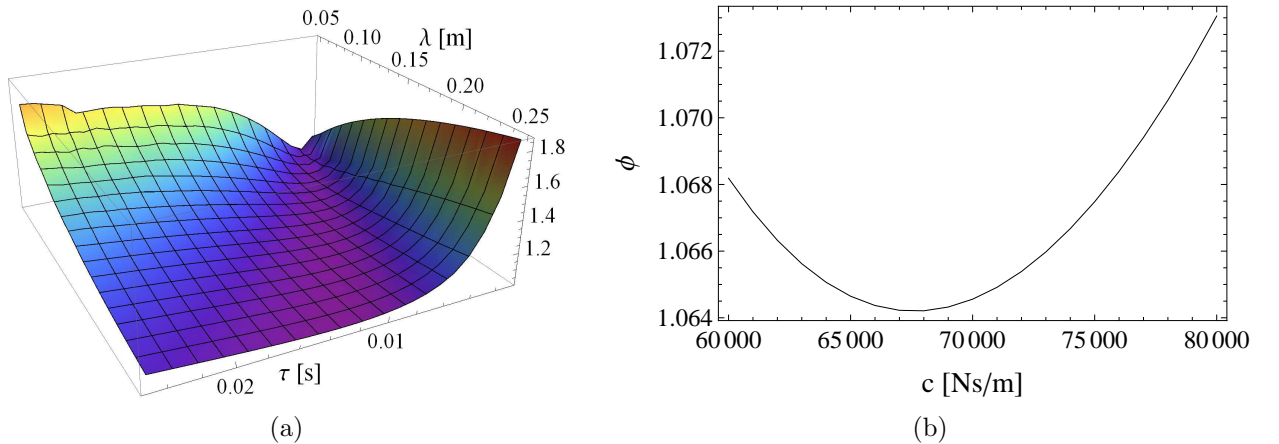

(a)   (b)

FIG. 10: The optimization map (a) of the non-linear system, and the optimization curve (b) of the linear one. In the optimization process, we set $t_1 = 15$ s , and $t_2 = 40$ s.

The results of the optimization process are shown in figures 10 for the non-linear system (10a), and, for comparison, for the linear one (10b). Interestingly, the non-linear system results show an optimum flat valley, allowing to achieve significantly optimized results with several sets of the design parameters τ and λ, providing enhanced compliance to the different design requirements (i.e. geometrical or material restrictions).

14

	Non-Linear	Linear
Parameters	$\tau = 0.013$ s $\lambda = 0.25$ m	$c = 68000$ $\frac{\text{Ns}}{\text{m}}$
F_M^i [N]	80255	85271
F_{rms}^i [N]	16313	17342

TABLE II: Comparison between non-linear and linear optimized system results.

A numerical comparison in terms of optimization results is found in Table II Interestingly, the non-linear behavior of the RLRB device allows to reduce both F_M^i and F_{rms}^i of about 6.3%, compared to the linear system. Such a result is also shown in figures 11 where the displacement time history and spectral analysis is shown for both the systems, compared to the earthquake data. The smoother behavior of the non-linear system shown in fig. 11a (blue line) compared to the linear system (red line) clearly entails lower inertial effects, and in turn lower stresses for the structural elements. Similarly, from fig. 11b, we observe that, although both the systems are able to filter the high frequency spectrum of the seismic event, the non-linear device (blue curve) still behaves better than the linear one (red curve) even close to ω_1.
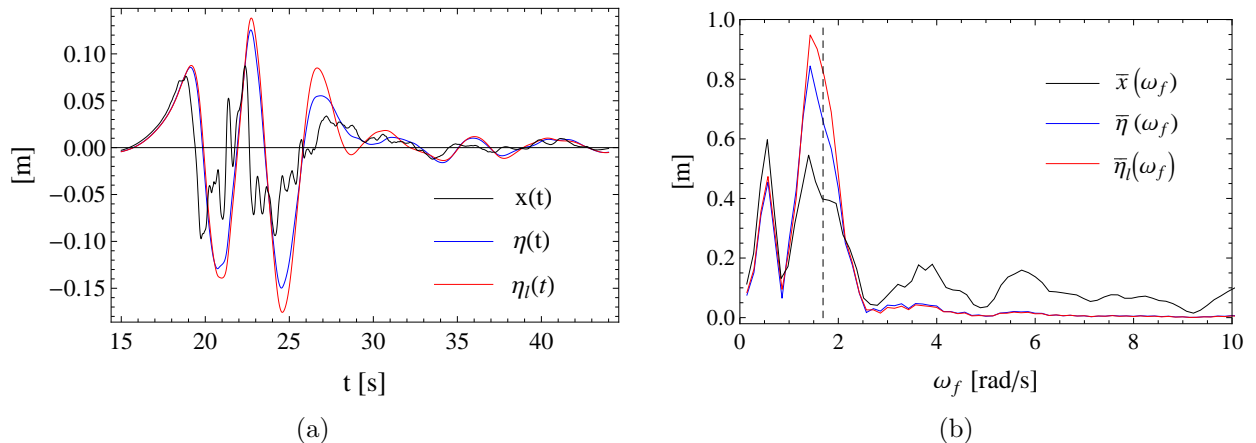

FIG. 11: The time history (a) and spectral analysis (b) of: the Central Italy heartquake 2016 (black curves); the inertial mass dispacement η for the non-linear (blue curves) and linear systems (red curves). The dashed line in (b) represent the system first natural frequency ω_1.

V. CONCLUSIONS

We investigated the dynamic behavior of RLRB seismic isolators, in which the viscoelastic rolling friction between the rigid cylinders and the rubber layers leads to a non-linear damping behavior. We found that the viscoelastic damping force is a bell-shaped function of the relative velocity of the moving parts (the ground and the building). Specifically, increasing the realtive velocity, an increasing damping behavior is observed, up to e threshold

velocity value beyond which a degreasing damping force is reported. Such a strongly nonlinear trend is controlled by the viscoelastic material relaxation time, and the rigid cylinders spacing, which indeed dramatically affect the overall system behavior. Specifically, depending on whether the RLRB operating condition lies on the increasing or decreasing portion of the damping curve, periodic, semi-periodic and aperidic system behavior can be observed. We investigate both the effect of the excitation frequency, as well as the specific set of parameters.

A real seismic event has been numerically reproduces in order to test the model, based on the Central Italy earthquake of October 2016. Indeed, an optimization procedure has been performed to minimize a performance index taking into account both the maximum instantaneous value and the root mean square value of the inertial loads history. Similarly, the behavior of an equivalent linearized system is investigated for comparison. Results show that the non-linear system is able to sufficiently reduce both the instantaneous and averaged inertial load value with respect to the linear system, opening the path to further deeper investigation on similar devices. Indeed, different sources of nonlinearity in RLRB devices will be further investigated.

[1] Starosvetsky, Y., & Gendelman, O. V. (2009). Vibration absorption in systems with a nonlinear energy sink: nonlinear damping. Journal of Sound and Vibration, 324(3-5), 916-939.

[2] Gendelman, O. V. (2012). Analytic treatment of a system with a vibro-impact nonlinear energy sink. Journal of Sound and Vibration, 331(21), 4599-4608.

[3] Gendelman, O. V., & Alloni, A. (2015). Dynamics of forced system with vibro-impact energy sink. Journal of Sound and Vibration, 358, 301-314.

[4] Samani, F. S., & Pellicano, F. (2009). Vibration reduction on beams subjected to moving loads using linear and nonlinear dynamic absorbers. Journal of Sound and Vibration, 325(4-5), 742-754.

[5] Samani, F. S., & Pellicano, F. (2012). Vibration reduction of beams under successive traveling loads by means of linear and nonlinear dynamic absorbers. Journal of Sound and Vibration, 331(10), 2272-2290.

[6] Samani, F. S., Pellicano, F., & Masoumi, A. (2013). Performances of dynamic vibration absorbers for beams subjected to moving loads. Nonlinear Dynamics, 73(1-2), 1065-1079.

[7] Bukhari, M. A., Barry, O., & Tanbour, E. (2018). On the vibration analysis of power lines with moving dampers. Journal of vibration and control, 24(18), 4096-4109.

[8] Myslimaj, B., Gamble, S., Chin-Quee, D., Davies, A., & Breukelman, B. (2003, September). Base isolation technologies for seismic protection of museum artifacts. In The 2003 IAMFA Annual Conference in San Francisco, California. San Francisco, CA: IAMFA.

[9] De la Cruz, S. T., López-Almansa, F., & Oller, S. (2007). Numerical simulation of the seismic behavior of building structures equipped with friction energy dissipators. Computers & Structures, 85(1-2), 30-42.

[10] Foti, D., Diaferio, M., & Nobile, R. (2013). Dynamic behavior of new aluminum–steel energy dissipating devices. Structural Control and Health Monitoring, 20(7), 1106-1119.

[11] Harvey Jr, P. S., & Kelly, K. C. (2016). A review of rolling-type seismic isolation: Historical development and future directions. Engineering Structures, 125, 521-531.

[12] Harvey Jr, P. S., & Gavin, H. P. (2015). Assessment of a rolling isolation system using reduced

order structural models. Engineering Structures, 99, 708-725.

[13] Casey, C. D., Harvey Jr, P. S., & Song, W. (2018). Multi-unit rolling isolation system arrays: Analytical model and sensitivity analysis. Engineering Structures, 173, 656-668.

[14] Miyamoto, K., Sato, D., & She, J. (2018). A new performance index of LQR for combination of passive base isolation and active structural control. Engineering Structures, 157, 280-299.

[15] Harvey Jr, P. S., & Gavin, H. P. (2013). The nonholonomic and chaotic nature of a rolling isolation system. Journal of Sound and Vibration, 332(14), 3535-3551.

[16] Harvey Jr, P. S., Wiebe, R., & Gavin, H. P. (2013). On the chaotic response of a nonlinear rolling isolation system. Physica D: Nonlinear Phenomena, 256, 36-42.

[17] Lin, T. W., Chern, C. C., & Hone, C. C. (1995). Experimental study of base isolation by free rolling rods. Earthquake engineering & structural dynamics, 24(12), 1645-1650.

[18] Foti D, Kelly JM. Experimental analysis of a model isolated at the base with rubber-layer roller bearing (RLRB). Euro Earthquake Eng 1996;10:3–13.

[19] Muhr AH, Sulong M, Thomas AG. Rolling-ball rubber-layer isolators. J Nat Rubber Res 1997;12(4):199–214.

[20] Muhr AH, Bergamo G. Shaking table tests on rolling-ball rubber-layer isolation system. In: 14th European conference on earthquake engineering. p. 5703–10.

[21] Guerreiro, L., Azevedo, J., & Muhr, A. H. (2007). Seismic tests and numerical modeling of a rolling-ball isolation system. Journal of Earthquake Engineering, 11(1), 49-66.

[22] Foti D, Catalan Goni A, Vacca S. On the dynamic response of rolling base isolation systems. Struct Control Health Monit 2013;20:639–48. http://dx.doi. org/10.1002/stc.1538.

[23] Fiore, A., Marano, G. C., & Natale, M. G. (2016). Theoretical prediction of the dynamic behavior of rolling-ball rubber-layer isolation systems. Structural Control and Health Monitoring, 23(9), 1150-1167. http://dx.doi.org/10.1002/stc.1830.

[24] Menga, N., Foti, D., & Carbone, G. (2017). Viscoelastic frictional properties of rubber-layer roller bearings (RLRB) seismic isolators. Meccanica, 52(11-12), 2807-2817.

[25] Carbone, G., & Mangialardi, L. (2008). Analysis of the adhesive contact of confined layers by using a Green's function approach. Journal of the Mechanics and Physics of Solids, 56(2), 684-706.

[26] Menga, N., Afferrante, L. and Carbone, G., Effect of thickness and boundary conditions on the behavior of viscoelastic layers in sliding contact with wavy profiles, The Journal of the Mechanics and Physics of Solids 2016;95: 517-529.

[27] Menga, N., Afferrante, L., Demelio, G. P., & Carbone, G. Rough contact of sliding viscoelastic layers: numerical calculations and theoretical predictions. Tribology International, 2018; 122:67-75.

[28] Menga, N., L. Afferrante, and G. Carbone. Adhesive and adhesiveless contact mechanics of elastic layers on slightly wavy rigid substrates. International Journal of Solids and Structures 2016;88:101-109.

[29] Menga, N., Putignano, C., Afferrante, L., & Carbone, G. (2019). The Contact Mechanics of Coated Elastic Solids: Effect of Coating Thickness and Stiffness. Tribology Letters, 67(1), 24.

[30] Menga, N. (2019). Rough frictional contact of elastic thin layers: the effect of geometrical coupling. International Journal of Solids and Structures.

[31] Demidovich, B. P., & Maron, I. A. (1963). Fundamentals of computational mathematics. Fizmatgiz, Moscow.

[32] Putignano, C., Carbone, G., & Dini, D. (2016). Theory of reciprocating contact for viscoelastic solids. Physical Review E, 93(4), 043003.

[33] Preumont, A., & Seto, K. (2008). Active control of structures. John Wiley & Sons.

[34] Ng, C. L., & Xu, Y. L. (2007). Semi-active control of a building complex with variable friction dampers. Engineering Structures, 29(6), 1209-1225.

[35] Yanik, A., Aldemir, U., & Bakioglu, M. (2014). A new active control performance index for vibration control of three-dimensional structures. Engineering Structures, 62, 53-64.

[36] Sadek, F., & Mohraz, B. (1998). Semiactive control algorithms for structures with variable dampers. Journal of Engineering Mechanics, 124(9), 981-990.

[37] http://itaca.mi.ingv.it/ItacaNet/CadmoDriver?_action_do_single=1&_criteria=CZ003AND%20CZ003AN 20161030_0000029%27CZ001%3d%20AZ013location_codeIAZ00200%27CZ001%3d%20AZ008net_codeIAZ